Chapter 11
Emulating Neutron Irradiation Effects with Ions

Radiation effects research is conducted with a variety of energetic particles: neutrons, electrons, light ions, and heavy ions. Energetic ions can be used to understand the effects of neutron irradiation in reactor components, and interest in this application of ion irradiation has grown in recent years for several reasons that include the avoidance of high residual radioactivity and a decline in the availability of test reactors for materials irradiation. The damage state and microstructure resulting from ion irradiation, and thus the degree to which ion irradiation emulates neutron irradiation, depend principally on the particle type and the damage rate. This chapter will begin with a brief review of the damage function, primary recoil spectrum, and efficiency of defect production for various particle types. Effects of particle type on both microstructure and microchemistry will be discussed, followed by the effects of the irradiated microstructure on mechanical properties. The roles of dose, dose rate, and temperature parameters and the constraints on parameter space by each particle source will be discussed and compared against the effects of neutron irradiation.

11.1 Motivation for Using Ion Irradiation as a Surrogate for Neutron Irradiation

In the 1960s and 1970s, heavy ion irradiation was developed for the purpose of simulating neutron damage in support of the fast breeder reactor program [1–3]. Ion irradiation and simultaneous He injection have also been used to simulate the effects of 14 MeV neutron damage in conjunction with the fusion reactor engineering program. The application of ion irradiation (defined here as any charged particle, including electrons) to the study of neutron irradiation damage is of interest to the light water reactor community to address issues such as stress corrosion cracking (SCC) of core materials that are affected by irradiation [4–6]. Ion irradiation is also being used to understand the irradiated microstructure of reactor pressure vessel steels, Zircaloy fuel cladding, and materials for advanced reactor concepts.

G.S. Was, *Fundamentals of Radiation Materials Science*,
DOI 10.1007/978-1-4939-3438-6_11

There is significant incentive to use ion irradiation to study neutron damage as this technique has the potential for yielding answers on basic processes in addition to the potential for enormous savings in time and money. Neutron irradiation experiments are not amenable to studies involving a wide range of conditions, which is precisely what is required for investigations of the basic damage processes. Radiation damage experiments using ion irradiation allow for easy variation of the irradiation parameters such as dose, dose rate, and temperature over a wide range of values.

Typical neutron irradiation experiments in test reactors require years of incore exposure to reach appreciable fluence levels for accelerated post-irradiation testing. This is accompanied by at least another year of capsule design and preparation as well as disassembly and cooling. Analysis of microchemical changes using techniques such as Auger electron spectroscopy (AES) and atom probe tomography (APT), microstructural changes by energy dispersive spectroscopy via scanning transmission electron microscopy (STEM-EDS), and mechanical property or SCC evaluation can take several additional years because of the precautions, special facilities, and instrumentation required for handling radioactive samples. The result is that a single cycle from irradiation through microanalysis and mechanical property/SCC testing may take between three and five years. Such a long cycle length does not permit for iteration on irradiation or material conditions that is critical in any experimental research program. The long lead time required for design and irradiation also reduces flexibility in altering irradiation programs as new data become available. Because of the long cycle time, the requirement of special facilities and special sample handling, the costs for neutron irradiation experiments are very high.

In contrast to neutron irradiation, ion irradiation enjoys considerable advantages in both cycle length and cost. Ion irradiations of any type rarely require more than several tens of hours to reach damage levels in the 1–10 dpa range. Ion irradiation produces little or no residual radioactivity, allowing handling of samples without the need for special precautions. These features translate into significantly reduced cycle length and cost. The challenge is then to verify the equivalency of the results of neutron and ion irradiation.

The key question that needs to be answered is how do results from neutron and charged particle irradiation experiments compare? How, for example is one to compare the results of a component irradiated in-core at 288 °C to a fluence of 1×10^{21} n/cm^2 ($E > 1$ MeV) over a period of 8.5 months, with an ion irradiation experiment using 3 MeV protons at 400 °C to 1 dpa (displacements per atom) at a dose rate of 10^{-5} dpa/s ($\sim$1 day), or 5 MeV Ni^{++} at 500 °C to 10 dpa at a dose rate of 5×10^{-3} dpa/s ($\sim$1 h)? The first question to resolve is the measure of radiation effect. In the irradiation-assisted stress corrosion cracking (IASCC) problem in LWRs, concern has centered on two effects of irradiation: *segregation* of major alloying elements or impurities to grain boundaries, which then cause embrittlement or enhance the intergranular stress corrosion cracking (IGSCC) process, and *hardening* of the matrix that results in localized deformation and embrittlement. The appropriate *measure* of the radiation effect in the former case would then be the

alloy concentration at the grain boundary or the amount of impurity segregated to the grain boundary. This quantity is measurable by analytical techniques such as AES or STEM-EDS. For the latter case, the *measure* of the radiation effect would be the nature, size, density, and distribution of dislocation loops, black dots, and the total dislocation network, and how they impact the deformation of the alloy. Hence, specific and measurable effects of irradiation can be determined for both neutron and ion irradiation experiments.

The next concern is determining how ion irradiation translates into the environment describing neutron irradiation. That is, what are the irradiation conditions required for ion irradiation to yield the same *measure* of radiation effect as that for neutron irradiation? This is the key question; for in a post-irradiation test program, it is only the *final state* of the material that is important in the determination of equivalence, and not the path taken. Therefore, if one could devise ion irradiation experiments that yielded the same *measures* of irradiation effects as observed in neutron irradiation experiments, then the data obtained in post-irradiation experiments will be equivalent. In such a case, ion irradiation experiments can provide a direct substitute for neutron irradiation. While neutron irradiation will likely be required to qualify materials for reactor application, ion irradiation provides a low cost and rapid means of elucidating mechanisms and screening materials for the most important variables.

11.2 Review of Aspects of Radiation Damage Relevant to Ion Irradiation

The first challenge in determining the equivalence between the measure of radiation effect in charged particle and neutron irradiation is the use of a common dose unit. Recall from the introduction that irradiated material properties can be more successfully compared using dpa as a measure of exposure. The basic (measurable) dose unit for neutron irradiation is the fluence in (n/cm^2) above some energy ($E > x$ MeV), where x is the energy threshold. For charged particles, it is the integrated current or charge in units of Q/cm^2. Both of these measures can be converted to dose in units of dpa and dose rate as dpa/s using one of several models for the determination of dpa, as described in Chap. 2. A fundamental difference between ion and neutron irradiation effects is the particle energy spectrum that arises due to the difference in how the particles are produced. Ions are produced in accelerators and emerge in monoenergetic beams with vary narrow energy widths. However, the neutron energy spectrum in a reactor extends over several orders of magnitude in energy, thus presenting a much more complicated source term for radiation damage. Figure 11.1 shows the considerable difference in neutron and ion energy spectra and also between neutron spectra in different reactors and at different locations within the reactor vessel.

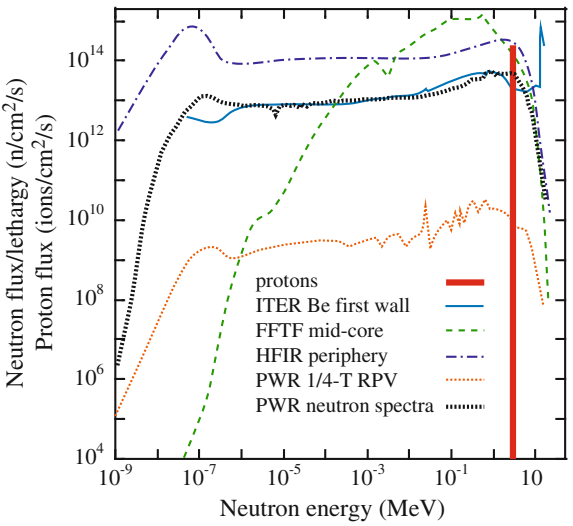

Fig. 11.1 Energy spectra of incident ions in a monoenergetic ion beam, and neutrons from a variety of reactor types (after [7])

Another major difference in the characteristics of ions and neutrons is their depth of penetration. As shown in Fig. 2.25 of Chap. 2, ions lose energy quickly because of high electronic energy loss, giving rise to a spatially non-uniform energy deposition profile caused by the varying importance of electronic and nuclear energy loss during the slowing down process. Their penetration distances range between 0.1 and 100 μm for ion energies that can practically be achieved by laboratory-scale accelerators or implanters. By virtue of their electrical neutrality, neutrons can penetrate very large distances and produce spatially flat damage profiles over many millimeters of material.

As discussed in Chap. 2, the total number of displacements per atom is given by the K–P [8] or NRT [9] models. This quantity provides an adequate measure of the number of displacements created by the incoming particle irrespective of the mass of the particle. In addition to dpa, the primary recoil spectrum describes the relative number of collisions in which an energy between T and $T + \mathrm{d}T$ is transferred from the primary recoil atom to other target atoms. The fraction of recoils between the displacement energy E_d, and T is given as, from Eq. (3.11):

$$P(E_\mathrm{i}, T) = \frac{1}{N} \int_{E_\mathrm{d}}^{T} \sigma(E_\mathrm{i}, T')\, \mathrm{d}T' \tag{11.1}$$

where N is the total number of primary recoils and $\sigma(E_\mathrm{i}, T')$ is the differential cross section for a particle of energy E_i to create a recoil of energy T', and E_d is the displacement energy. The recoil fraction is shown in Fig. 3.5, which reveals only a small difference between ions of very different masses.

But there is a substantial difference in the damage morphology between particles of different mass. Light ions such as electrons and protons will produce damage as

isolated Frenkel pairs or in small clusters while heavy ions and neutrons produce damage in large clusters (see Fig. 3.7). For 1 MeV particle irradiation of copper, half of the recoils for protons are produced with energies less than ~60 eV while the same number for Kr occurs at about 150 eV. Recoils are weighted toward lower energies because of the screened Coulomb potential that controls the interactions of charged particles. For an unscreened Coulomb interaction, the probability of creating a recoil of energy T varies as $1/T^2$. However, neutrons interact as hard spheres and the probability of creating a recoil of energy T is independent of recoil energy. In fact, a more important parameter describing the distribution of damage over the energy range is a combination of the fraction of defects of a particular energy and the damage energy. As described in Chap. 3, the *weighted average* recoil spectrum, $W(E_i, T)$, weights the primary recoil spectrum by the number of defects or the damage energy produced in each recoil:

$$W(E_i, T) = \frac{1}{E_D(E_i)} \int_{E_d}^{T} \sigma(E_i, T') E_D(T') \mathrm{d}T' , \tag{11.2}$$

$$E_D(E_i) = \int_{E_d}^{\hat{T}} \sigma(E_i, T') E_D(T') \mathrm{d}T' , \tag{11.3}$$

where $\hat{T}$ is the maximum recoil energy given by $\hat{T} = \gamma E_i = 4E_i M_1 M_2/(M_1 + M_2)^2$. As described in Chap. 3, for the extremes of Coulomb and hard sphere interactions, the weighted average recoil spectrum for each type of interaction is given as follows:

$$W_{\mathrm{Coul}}(E_i, T) = \frac{\ln T - \ln E_d}{\ln \hat{T} - \ln E_d} \tag{11.4a}$$

$$W_{\mathrm{HS}}(E_i, T) = \frac{T^2 - E_d^2}{\hat{T}^2} . \tag{11.4b}$$

Equations (11.4a) and (11.4b) are graphed in Fig. 3.6 for 1 MeV particle irradiations of copper. The Coulomb forces extend to infinity and slowly increase as the particle approaches the target, hence the slow increase with energy. In a hard sphere interaction, the particles and target do not *feel* each other until their separation reaches the hard sphere radius at which point the repulsive force goes to infinity. A screened Coulomb potential is most appropriate for heavy ion irradiation. Note the large difference in $W(E_i, T)$ between the various types of irradiations. While heavy ions come closer to reproducing the energy distribution of recoils of neutrons than do light ions, neither is accurate in the *tails* of the distribution. This does not mean that ions are poor simulations of radiation damage, but it does mean that damage is produced differently and this difference will need to be considered when designing an irradiation program that is intended to produce microchemical and microstructural changes that match those from neutron irradiation.

The actual number of defects that survive the displacement cascade and their spatial distribution in the solid will determine the effect on the irradiated microstructure. This topic was covered in Chaps. 3 and 7 by classification of defects according to their behavior in the solid. Figure 11.2 summarizes the effect of damage morphology from the viewpoint of the grain boundary and how the defect flow affects radiation-induced grain boundary segregation. Despite the equivalence in energy among the four particle types described in Fig. 3.7, the average energy transferred and the defect production efficiencies vary by almost two orders of magnitude! This is explained by the differences in the cascade morphology among the different particle types. Neutrons and heavy ions produce dense cascades that result in substantial recombination during the cooling or quenching phase. However, electrons are just capable of producing a few widely spaced Frenkel pairs that have a low probability of recombination. Protons produce small widely spaced cascades and many isolated FPs due to the Coulomb interaction, and therefore, fall between the extremes in displacement efficiency as defined by electrons and neutrons.

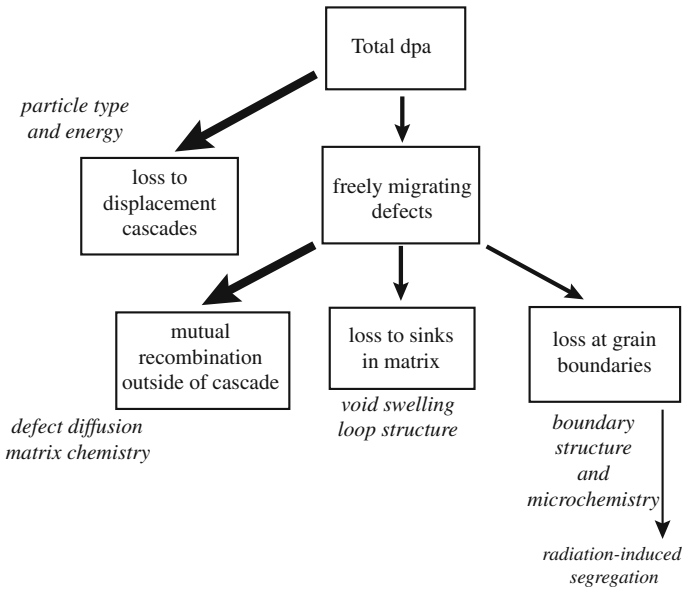

Fig. 11.2 History of point defects after creation in the displacement cascade

11.3 Particle-Type Dependence of RIS

We will focus on the comparison between four types of particle irradiation in order to outline a methodology for establishing equivalence between neutron and charged particle irradiation. We will further focus on radiation-induced segregation as the *measure* of the effect of irradiation in order to compare the particles. RIS is selected because it depends only on the action of point defects, and not on their agglomeration. The irradiation parameters for the four particle types are given in Table 11.1. Each experiment is characterized by the particle type, energy and irradiation temperature, reported dose rate, and reported total dose. The last column is the dose to reach a steady-state RIS profile using the Perk's model [11]. The columns labeled *reported* and *corrected* refer to RIS calculations using the nominal (*reported* value) and the efficiency-corrected (*corrected* value) dose rate, respectively. The displacement efficiency is calculated using Naundorf's model, described in Chap. 3.

A quantity of interest in RIS for LWR core materials is the amount of chromium depleted from the grain boundary, or the area inside the Cr concentration profile (Fig. 11.3). In non-LWR reactor systems, other elements may be of interest due to the potential for in-reactor precipitation. The appropriate measure of depletion is somewhat questionable. One could use the grain boundary chromium value as the measure of the extent of chromium depletion. Alternatively, the FWHM of the depletion profile has been used. In fact, both of these quantities are useful and can be obtained from measured depletion profiles. However, the area inside the Cr concentration profile represents changes to a volume of material and is more sensitive to changes in the profile shape than either the grain boundary value or the FWHM alone. The amount of Cr depletion is determined by integrating the concentration profile for that element with distance from the grain boundary:

$$M = \int_0^{l(t)} \left[C_A^0 - C_A(x,t)\right] \mathrm{d}x\,, \tag{11.5}$$

where M is the segregated area, C_A^0 is the bulk atom concentration, $C_A(x, t)$ is the atom concentration near the surface, and $l(t)$ is the half width of the depleted zone.

Figure 11.4(a, b) shows the amount of grain boundary chromium depletion as a function of irradiation dose (Fig. 11.4(a)) and time (Fig. 11.4(b)) for each of the four particles described in Table 11.1. The calculated values of Cr depletion for each of the particle types using *reported* and *corrected* dose rates, according to the freely migrating defect production efficiencies, are shown by the open and closed symbols, respectively. Since electrons are assumed to be 100 % efficient in producing defects available to affect segregation, there is no change in the segregated area after accounting for efficiency. However, there is a difference with protons, heavy ions, and neutrons, which amounts to a reduction in the amount of segregation. The difference is largest for neutrons and smallest for protons. The difference is a function of not only the displacement efficiency, but also the slope of the

Table 11.1 Comparison of irradiation parameters and RIS for different particle types (from [10])

Particle type	Energy (MeV)	Temp (°C)	Efficiency	Dose rate (dpa/s)		Total dose (dpa)		Dose to steady state[b] (dpa)	
				Reported	Corrected[a]	Reported	Corrected	Reported	Corrected
Electrons	1.0	450	1.0	2×10^{-3}	2×10^{-3}	10	10	28	28
Protons	3.4	360	0.2	7×10^{-6}	1×10^{-6}	1	0.2	7	3
Ni ions	5.0	500	0.04	5×10^{-3}	2×10^{-4}	10	0.4	25	7
Neutrons	Fission reactor	288	0.02	$\sim 5 \times 10^{-8}$	1×10^{-9}	1	0.02	4	1.4

[a]Efficiency-corrected value
[b]As calculated by the Perks model [11] for RIS

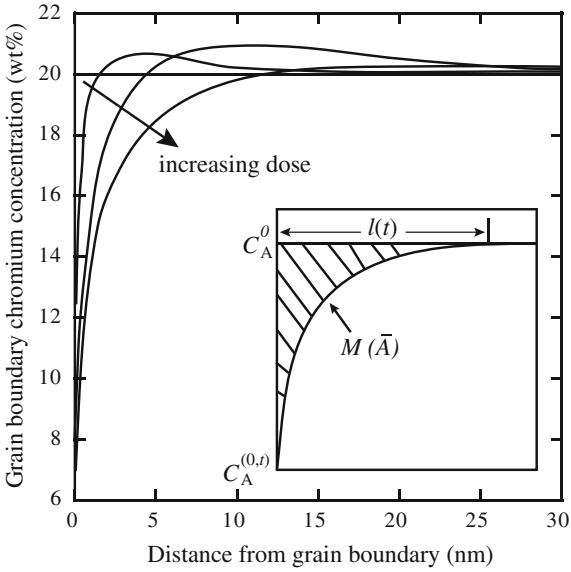

Fig. 11.3 Definition of the segregated area, M in a quantitative assessment of RIS

dose rate curves. Nevertheless, substantial differences result in the expected amounts of grain boundary segregation when the displacement efficiency is taken into account.

Figure 11.5(a) shows the calculated amount of Cr depletion as a function of temperature for several displacement rates at *steady state*. Steady state is reached at different dose levels for each experiment. At a given displacement rate, the segregated area peaks at some intermediate temperature and falls off at both higher and lower temperatures. This is due to the dominance of recombination at low temperatures and back diffusion at high temperatures [10]. Also note that the effect of a decreasing displacement rate is to shift the curves to higher maxima at lower temperatures. For a given dose, a lower displacement rate yields lower steady-state defect concentrations, reducing the number of defects lost to recombination, and shifting the curve to lower temperatures while increasing the degree of segregation. Figure 11.5(a) also shows the effect of three of the four parameters defining an experiment: particle type, temperature, and dose rate. It does not show the effect of dose since this is a steady-state result that is achieved at different doses for each of the experiments described in Table 11.1.

Figure 11.5(b) shows the dose required to reach steady state as a function of temperature and dose rate. Each of the experiments is plotted for both the reported and the corrected displacement rates. Note the large difference in the dose to reach steady state between electrons and neutrons. In general, irradiation at a lower dpa rate will result in a lower dose to reach steady state and the difference is greatest for this comparison. Correspondingly, proton and heavy ion irradiation fall between neutrons and electrons for the experiments described in Table 11.1. This can be

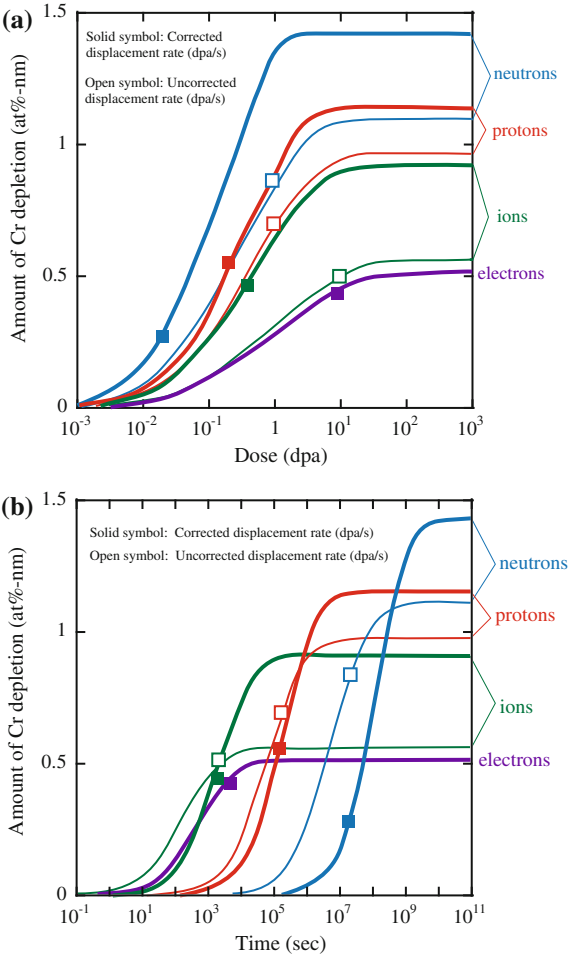

Fig. 11.4 Chromium depletion versus (**a**) dose and (**b**) irradiation time, for several particle types (thin line) and the effect of correcting for particle efficiency (heavy line) (after [10]). Symbols refer to conditions in Table 11.1

understood by considering the chemical rate equations given in Eq. (5.1), where the first term is the production rate, the second is the loss by mutual recombination, and the third is the loss by annihilation of defects at sinks. At steady state, $C_{i,v} \propto K_0^{1/2}$ at low temperature and $C_{i,v} \propto K_0$ at high temperature (see Chap. 5). So, the resulting point defect concentrations are strong functions of the production rate.

Figure 11.6 shows a plot of segregation as a function of temperature for particles with displacement rates characteristic of their sources. Note that the temperature at which segregation is a maximum (concentration is a minimum) shifts to higher values with increasing dose rate. This is due to the trade-off between temperature and dose rate. The temperature-dose rate interdependence for stainless steel over a wide range of temperatures and dose rates is shown in Fig. 11.7. Also noted are the regions in which reactor irradiation by neutrons, and where proton and Ni ion

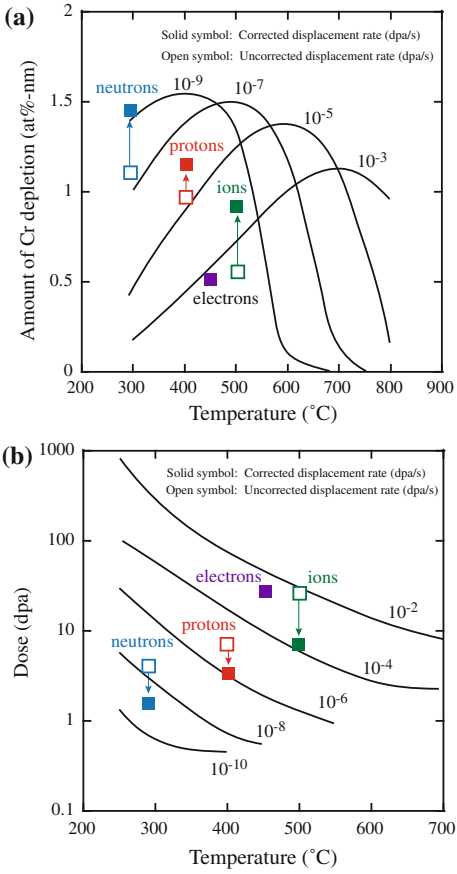

Fig. 11.5 (**a**) Chromium depletion and (**b**) dose to reach steady state as a function of temperature, dose rate, and particle efficiency (after [10]). Symbols refer to conditions in Table 11.1

irradiations occur. This graph explains why the experiments conducted at the highest dose rates are also conducted at the highest temperatures.

A simple method for examining the trade-off between dose rate and temperature in comparing irradiation effects from different particle types is found in the invariance requirements discussed in Chap. 8. For a given change in dose rate, we would like to know what change in temperature (at the same dose) is required to cause the same number of defects to be absorbed at sinks. The number of defects per unit volume that are lost to sinks up to time τ is given as:

$$N_{Sj} = \int_0^{\tau} k_{Sj}^2 C_j \mathrm{d}t, \tag{11.6}$$

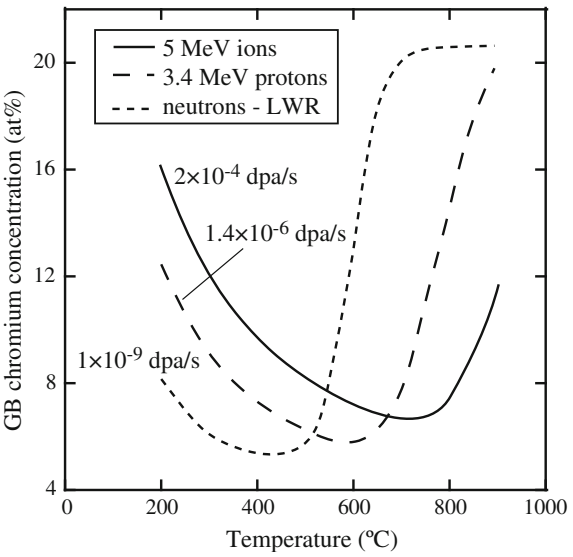

Fig. 11.6 Dependence of grain boundary chromium concentration on temperature for particles with various dose rates and defect generation efficiencies (after [10])

and the ratio of vacancy loss to interstitial loss is given as:

$$R_S = \frac{N_{Sv}}{N_{Si}}, \tag{11.7}$$

where j = v or i, and k_S^2 is the sink strength. The quantity N_S is important in describing microstructure development involving total point defect flux to sinks (e.g., RIS). The number of defects per unit volume that have recombined up to time τ is given by:

$$N_R = K_{iv} \int_0^{\tau} C_i C_v dt, \tag{11.8}$$

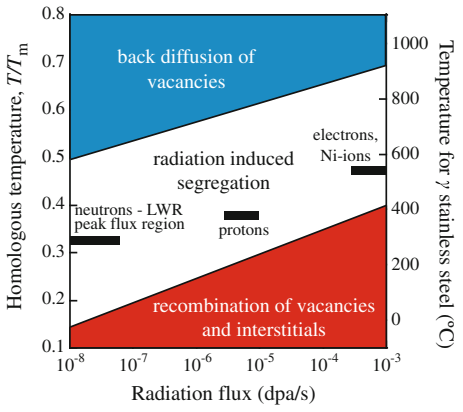

Fig. 11.7 Relation between temperature and dose rate in the context of radiation-induced segregation, and the locations of neutron, proton, and nickel ion irradiations

where K_{iv} is the vacancy–interstitial recombination coefficient. N_R is the relevant quantity for the growth of defect aggregates such as voids and loops that require partitioning of point defects to allow growth.

The invariance requirements can be used to prescribe an ion irradiation temperature-dose rate combination that simulates neutron radiation. We take the example of irradiation of stainless steel under typical boiling water reactor (BWR) core irradiation conditions of $\sim 4.5 \times 10^{-8}$ dpa/s at 288 °C. If we were to conduct a proton irradiation with a characteristic dose rate of 7.0×10^{-6} dpa/s, then using Eq. (8.158) with a vacancy formation energy of 1.9 eV and a vacancy migration energy of 1.3 eV, the experiment will be invariant in N_S with the BWR core irradiation (e.g., RIS), for a proton irradiation at 400 °C. Similarly, using Eq. (8.162), an irradiation temperature of 300 °C will result in an invariant N_R (e.g., swelling or loop growth). For a Ni^{++} ion irradiation at a dose rate of 10^{-3} dpa/s, the respective temperatures are 675 °C (N_S invariant) and 340 °C (N_R invariant). In other words, the temperature "shift" due to the higher dose rate is dependent on the microstructure feature of interest. Also, with increasing difference in dose rate, the ΔT between proton and ion irradiation increases substantially. The nominal irradiation temperatures selected for proton irradiation, 360 °C and for Ni^{++} irradiation, 500 °C represent compromises between the extremes for invariant N_S and N_R.

11.4 Advantages and Disadvantages of the Various Particle Types

Each particle type has its advantages and disadvantages for use in the study or emulation of radiation effects. Common disadvantages of charged particle beams are the lack of transmutation reactions and the need to use a raster-scanned beam. With the exception of some minor transmutation reactions that can occur with light ion irradiation, charged particles do not reproduce the types of transmutation reactions that occur in reactor core materials due to interaction with neutrons. The most important of these is the production of He by transmutation of Ni or B (See Sect. 8.4.5). But a second consideration is that of a raster-scanned beam in which any volume element of the target is exposed to the beam for only a fraction of the raster-scan cycle. For a typical beam scanner and beam parameters, the fraction of time that any particular volume element in the solid is being bombarded is ~ 0.025. Thus, the instantaneous dose rate during the *beam-on* portion of the cycle is 40 times that of the average (Fig. 11.8). The result is that the defect production rate is very high and defects can anneal out in the remaining 0.975 portion of the cycle before the beam again passes through the volume element. As such, the effective defect production rate in raster-scanned systems will be less and must be accounted for.

While one objective of ion irradiation is to emulate the effect of neutrons, a second is to understand basic physical radiation damage processes, for which neutron irradiation is often less well suited. While ion irradiation can be conducted

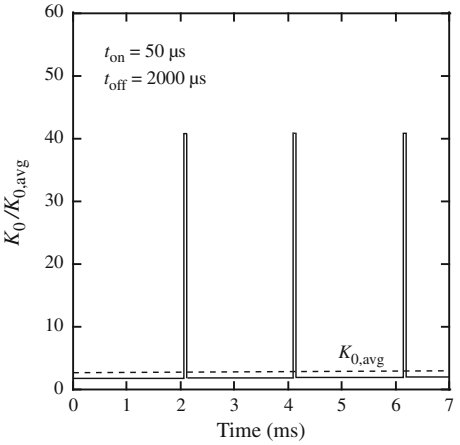

Fig. 11.8 The effect of a raster-scanned beam on the instantaneous production rate of point defects with the same time averaged rate as a continuous source (after [12])

with excellent control over temperature, dose rate, and total dose, such control is a challenge to reactor irradiations. For example, instrumented tubes with active temperature control are expensive to design, build, and operate. Even so, frequent power changes can be difficult to handle as the flux–temperature relationship will change and this can result in artifacts in the irradiated microstructure (see Sect. 8.3.11 and Fig. 8.57). On the other hand, cheaper "rabbit" tube irradiations use passive gamma heating and temperatures are not known with any certainty. Similarly, doses and dose rates are most often determined by neutronic models of the core locations and are not verifiable. As such, ion irradiations enjoy the advantage of better control and verification of irradiation conditions as compared to neutron irradiation. Table 11.2 provides a list of advantages and disadvantages for each of three particle types: electrons, heavy ions, and light ions (protons), and they are discussed in detail in the following sections.

11.4.1 Electrons

Electron irradiation is easily conducted in a high-voltage transmission electron microscope and as such, it uses a rather simple ion source, that being either a hot filament or a field emission gun. An advantage is that the same instrument used for irradiation damage can be used to image the damage. Another advantage is that the high dose rate requires very short irradiation time, but this will also require a large temperature shift as explained in the previous section.

There are several disadvantages to electron irradiation using a TEM. First, energies are generally limited to 1 MeV. This energy is sufficient to produce an isolated Frenkel pair in transition metals, but not cascades. The high dose rate requires high temperatures that must be closely monitored and controlled, which is difficult to do precisely in a typical TEM sample stage. Another drawback is that

Table 11.2 Advantages and disadvantages of irradiations with various particle types (after [12])

Advantages	Disadvantages
Electrons	
Relatively "simple" source—TEM	Energy limited to ~1 MeV
Uses standard TEM sample	No cascades
High dose rate—short irradiation times	Very high beam current (high dpa rate) leading to large temperature shift relative to neutrons
	Poor control of sample temperature
	Strong "Gaussian" shape (non-uniform intensity profile) to beam
	No transmutation
Heavy Ions	
High dose rate—short irradiation times	Very limited depth of penetration
High T_{avg}	Strongly peaked damage profile
Cascade production	Very high beam current (high dpa rate) leading to large temperature shift relative to neutrons
	No transmutation
	Potential for composition changes at high dose via implanted ion
Protons	
Accelerated dose rate—moderate irradiation times	Minor sample activation
Modest ΔT required	Smaller, widely separated cascades
Good depth of penetration	No transmutation
Flat damage profile over tens of μm	Damage rate limited by heat removal

since irradiations are often conducted on thin foils, defects are created in close proximity to the surface and their behavior may be affected by the presence of the surface. Perhaps, the most serious drawback is the Gaussian shape to the electron beam that can give rise to strong dose rate gradients across the irradiated region. Figure 11.9 shows the composition profile of copper around a grain boundary in Ni–39 %Cu following electron irradiation. Note that while there is local depletion at the grain boundary (as expected), the region adjacent to the minimum is strongly enriched in copper due to the strong defect flux *out* of the irradiated zone defined by the horizontal line below the spectrum. This outward-directed defect flux causes a reversal in the direction of segregation from that caused by a defect flux *to* the sink. Another often observed artifact in electron irradiation is very broad grain boundary enrichment and depletion profiles. Figure 11.10 shows that the enrichment profile for Ni and the depletion profiles for Fe and Cr in stainless steel have widths on the order of 75–100 nm, which is much greater than the 5–10 nm widths observed following neutron irradiation under similar conditions and all model simulations of

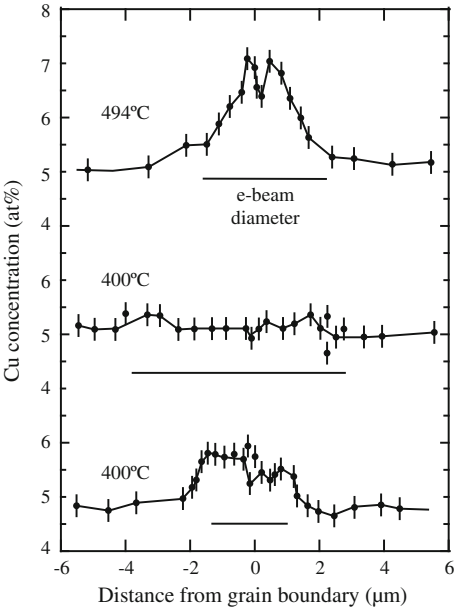

Fig. 11.9 Enrichment of copper at the grain boundary in Ni-39 %Cu. The enrichment is caused by the high-defect flux away from the irradiated region defined by the horizontal line (after [13])

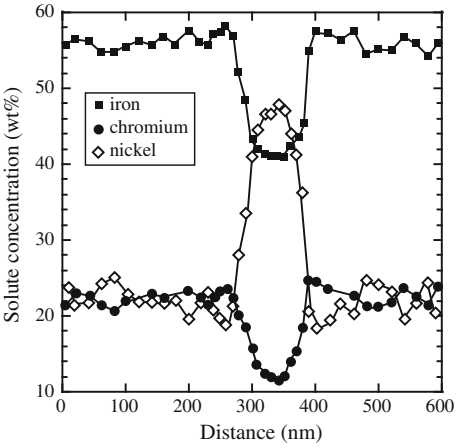

Fig. 11.10 Broad grain boundary enrichment and depletion profiles in Fe–20Cr–25Ni–0.75Nb–0.5Si following irradiation with electrons at 420 °C to 7.2 dpa (after [14])

radiation-induced segregation. A similar effect was noted by Wakai [15] in electron and D^+ irradiation of the same alloy in which it was observed that the segregation was much greater and narrower around the grain boundary in the deuteron-irradiated sample as compared to the electron irradiation (Fig. 11.11).

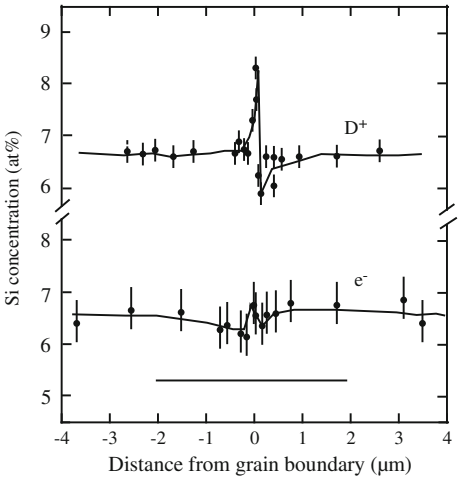

Fig. 11.11 Comparison of deuteron and electron irradiation showing the greater amount of Si segregation and the narrower profile for the deuteron irradiation (after [15])

11.4.2 Heavy Ions

Heavy ions enjoy the benefit of high dose rates resulting in the accumulation of high doses in short times. Also, because they are typically produced in the energy range of a few MeV, they are very efficient at producing dense cascades, similar to those produced by neutrons (Fig. 3.7). The disadvantage is that as with electrons, the high dose rates require large temperature shifts so that irradiations must be conducted at temperatures of order ~500 °C in order to create similar effects as neutron irradiation at ~300 °C. Clearly, there is not much temperature margin for studying neutron irradiations at high temperature since higher ion irradiation temperatures will cause annealing. Another drawback is the short penetration depth and the continuously varying dose rate over the penetration depth. Figure 11.12 shows

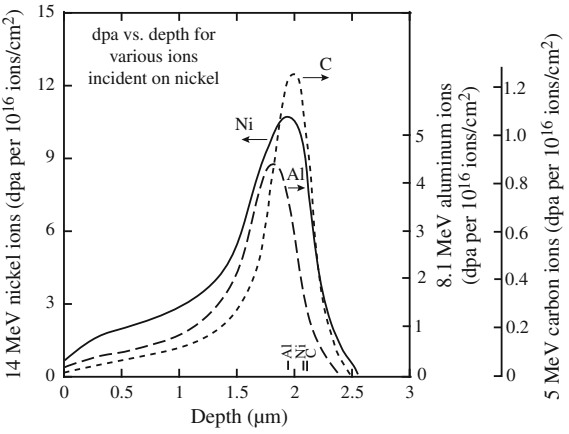

Fig. 11.12 Damage profiles for C, Al, and Ni irradiation of a nickel target at energies selected to result in the same penetration depth (after [16])

the damage profile for several heavy ions incident on nickel. Note that the damage rate varies continuously and peaks sharply at only 2 μm below the surface. As a result, regions at well-defined depths from the surface must be able to be reproducibly sampled in order to avoid dose or dose rate variations. Small errors (500 nm) made in locating the volume to be characterized can result in a dose that varies by a factor of two from the target value.

A problem that is rather unique to nickel ion irradiation of stainless steel or nickel-base alloys is that in addition to the damage they create, each bombarding Ni ion constitutes an interstitial. Figure 11.13(a) shows that 5 MeV Ni^{++} irradiation of a Fe–15Cr–35Ni alloy resulted in high swelling in the immediate subsurface region compared to that near the damage peak. As shown in Fig. 11.13(b), the Ni^{++} ions come to rest at a position just beyond the peak damage range. So even though the peak damage rate is about 3× that at the surface, swelling at that location is suppressed by about a factor of 5 compared to the surface [17]. The reason is that the bombarding Ni^{++} ions constitute interstitials and the surplus of interstitials near the damage peak results in a reduction of the void growth rate [18, 19]. In the dose rate-temperature regime where recombination is the dominant point defect loss mechanism, interstitials injected by Ni^{++} ion bombardment may never recombine

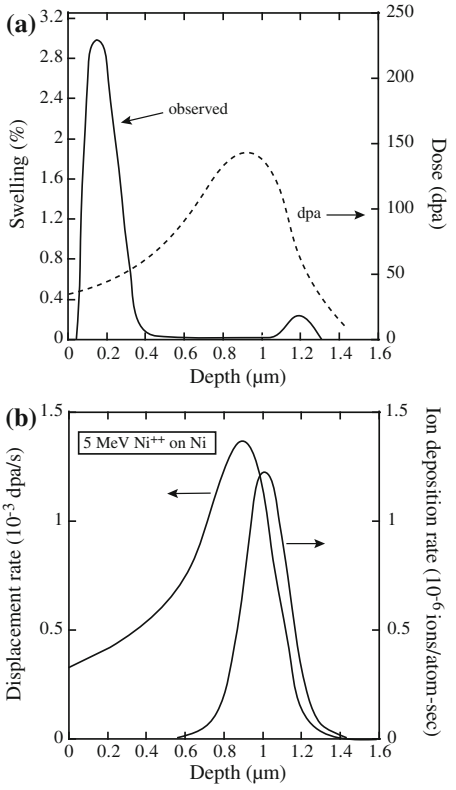

Fig. 11.13 (**a**) Subsurface swelling resulting from 5 MeV Ni^{++} ion irradiation of Fe–15Cr–35Ni at 625 °C (after [17]). (**b**) Displacement rate and ion deposition rate calculated for 5 MeV Ni^{++} on nickel (after [18])

since there is no corresponding vacancy production. Therefore, injected interstitials comprise a larger fraction of the point defects absorbed at sinks whenever the fraction of point defects recombining is large, such as in the peak swelling regime.

11.4.3 Protons

In many ways, proton irradiation overcomes the drawbacks of electron and neutron irradiation. At only a few MeV, the penetration depth can exceed 40 μm and the damage profile is relatively flat such that the dose rate varies by less than a factor of 2 over several tens of μm. Further, the depth of penetration is sufficient to assess such properties as irradiation hardening through microhardness measurements and SCC through crack initiation tests such as the slow strain rate test. Figure 11.14 (and Fig. 2.25) shows schematics of 3.2 MeV proton and 5 MeV Ni^{++} damage profiles in stainless steel. Superimposed on the depth scale is a grain structure with a grain size of 10 μm. Note that with this grain size, there are numerous grain boundaries and a significant irradiated volume over which the proton damage rate is flat. The dose rate for proton irradiations is 2–3 orders of magnitude lower than that for electrons or ions, thus requiring only a modest temperature shift, but since it is still 10^2 to 10^3 times higher than neutron irradiation, modest doses can be achieved in a reasonably short irradiation time.

The advantages are that because of the small mass of the proton compared to heavy ions, the recoil energy is smaller and the resulting damage morphology is characterized by smaller, more widely spaced cascades than with ions or neutrons (see Fig. 3.7). Also, since only a few MeV are required to surmount the Coulomb barrier for light ions, there is also a minor amount of sample activation that increases with proton energy.

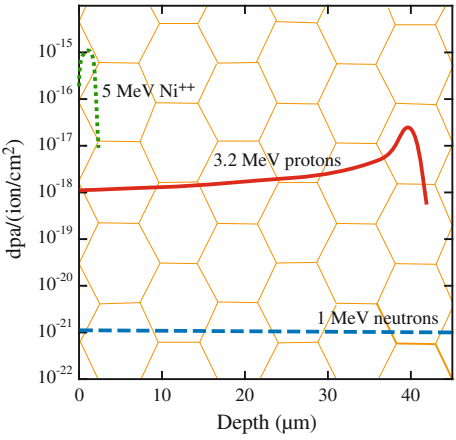

Fig. 11.14 Damage profiles for 3.2 MeV protons and 5 MeV Ni^{++} ions in stainless steel (after [12])

11.5 Irradiation Parameters for Particle Irradiations

In the process of setting up an ion irradiation experiment, a number of parameters that involve beam characteristics (energy, current/dose) and beam–target interaction must be considered. One of the most important considerations is the depth of penetration. Figure 11.15 shows the range versus particle energy for protons, helium ions, and nickel ions in stainless steel as calculated by SRIM [20]. The difference in penetration depth between light and heavy ions is over an order of magnitude in this energy range. Figure 11.16 shows how several other parameters describing the target behavior during proton irradiation vary with energy: dose rate, the time to reach 1 dpa, deposited energy, and the maximum permissible beam current (which will determine the dose rate and total dose) given a temperature limitation of 360 °C. With increasing energy, the dose rate at the surface decreases due to the drop in the elastic scattering cross section (Fig. 11.16(a)). Consequently, the time to reach a target dose level, and hence the length of an irradiation, increases rapidly (Fig. 11.16(b)). Energy deposition scales linearly with the beam energy, raising the burden of removing the added heat in order to control the temperature of the irradiated region (Fig. 11.16(c)). The need to remove the heat due to higher energies will limit the beam current for a specific target temperature (Fig. 11.16(d)) and a limit on the beam current (or dose rate) will result in a longer irradiation to achieve the specified dose. Figure 11.17 summarizes how competing features of an irradiation vary with beam energy, creating trade-offs in the beam parameters. For example, while greater depth is generally favored in order to increase the volume of irradiated material, the higher energy required leads to lower dose rates near the surface and higher residual radioactivity. For proton irradiation, the optimum energy range, achieved by balancing these factors, lies between 2 and 5 MeV as shown by the shaded region.

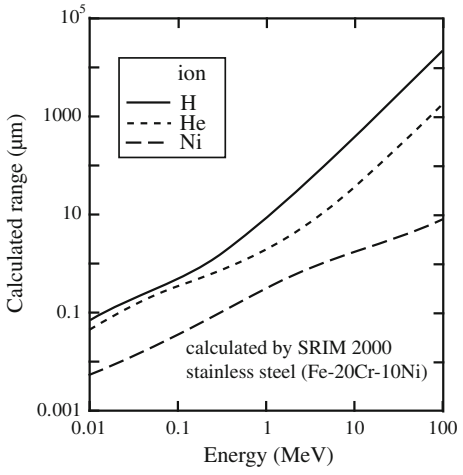

Fig. 11.15 Range of protons, helium atoms, and nickel ions in stainless steel as a function of ion energy (after [12])

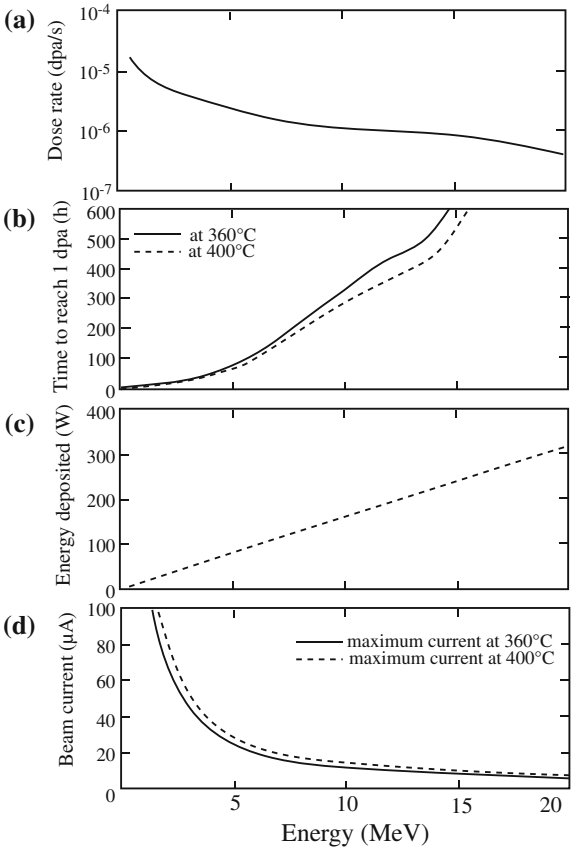

Fig. 11.16 Behavior of beam–target parameters as a function of beam energy for proton irradiation at 360 °C. (**a**) Dose rate, (**b**) time to reach 1 dpa, (**c**) energy deposition, and (**d**) beam current limit to maintain a sample temperature of 360 °C (after [12])

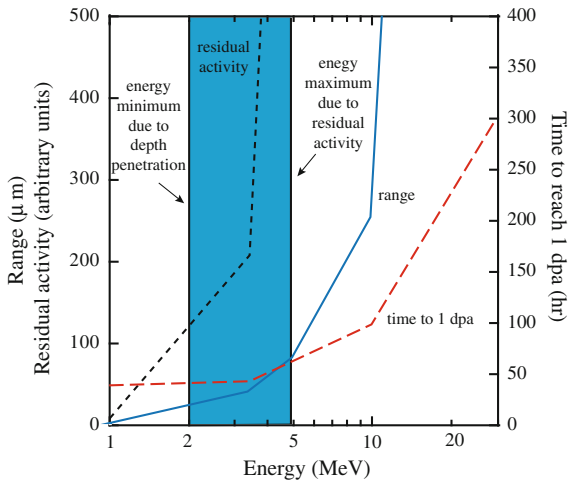

Fig. 11.17 Variation of ion range, residual activity, and time to reach 1 dpa as a function of proton energy (after [12])

11.6 Emulation of Neutron Irradiation Damage with Proton Irradiation

Proton irradiation has undergone considerable refinement as a radiation damage tool. Numerous experiments have been conducted and compared to equivalent neutron irradiation experiments in order to determine if proton irradiation can capture the effects of neutron irradiation on microstructure, microchemistry and hardening. In some cases, benchmarking exercises were conducted on the same native heat as neutron irradiation in order to eliminate heat-to-heat variations that may obscure comparison of the effects of the two types of irradiating particles. The following examples cover a number of irradiation effects on several alloys in an effort to demonstrate the capability of proton irradiation to capture the critical effects of neutron irradiation.

Figures 11.18, 11.19, 11.20, and 11.21 show direct comparisons of the *same* irradiation feature on the *same* alloy heats (commercial purity (CP) 304 and 316 stainless steels) following either neutron irradiation at 275 °C or proton irradiation at 360 °C to similar doses. Figure 11.18 compares the RIS behavior of Cr, Ni, and Si in a 316 stainless steel alloy following irradiation to approximately 1 dpa. Neutron irradiation results are in open symbols and proton irradiation results are in solid symbols. This dose range was chosen as an extreme test of proton irradiation to capture the "W"-shaped chromium depletion profile caused by irradiation of a microstructure-containing grain boundary chromium enrichment prior to irradiation. Note that the two profiles trace each other extremely closely both in magnitude and in spatial extent. The agreement extends across all three elements.

Figure 11.19 shows the agreement in the dislocation microstructure as measured by the dislocation loop size distribution (Fig. 11.19(a)) and the size and number density of dislocation loops (Fig. 11.19(b)) for 304 SS and 316 SS. Note that the main features of the loop size distributions are captured by both irradiations; sharply peaked distribution in the case of 304 SS and a flatter distribution with a tail for the

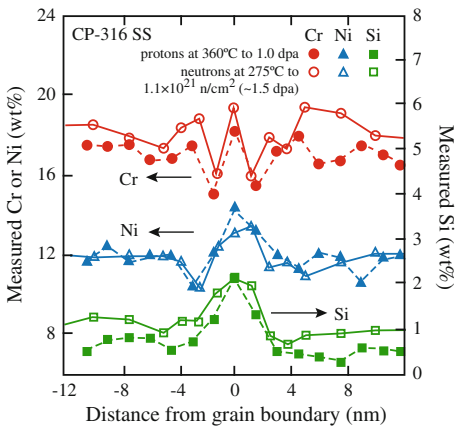

Fig. 11.18 Comparison of grain boundary segregation of Cr, Ni, and Si in commercial purity 316 stainless steel following irradiation with either protons or neutrons to similar doses (after [21])

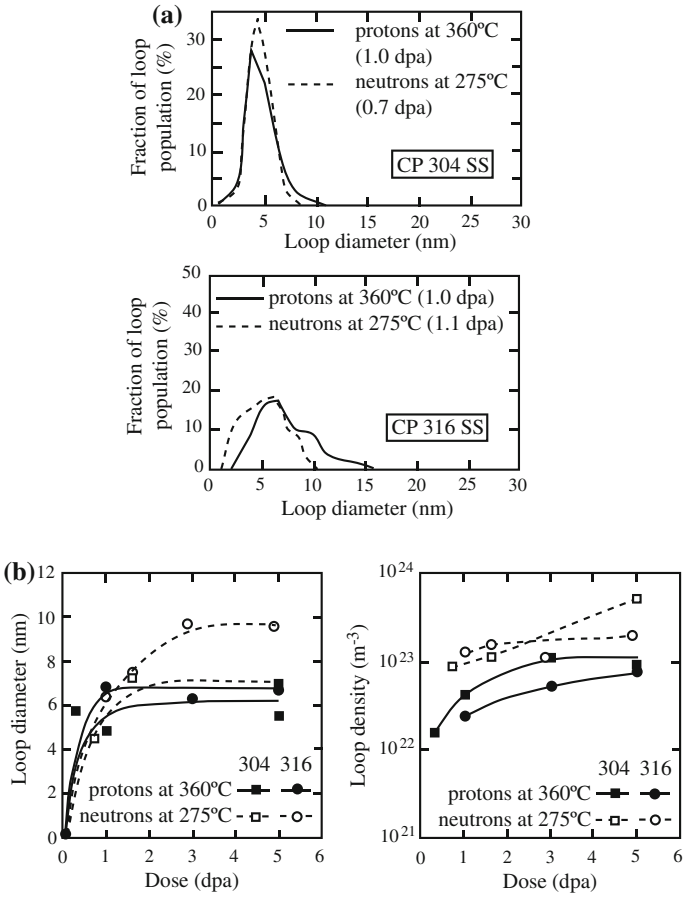

Fig. 11.19 Comparison of (**a**) loop size distributions and (**b**) loop diameter and loop number density for commercial purity 304 and 316 stainless steels irradiated with neutrons or protons to similar doses (after [21])

case of 316 SS. The agreement in loop size is good for the 304 SS alloy, while loops are smaller for the proton-irradiated 316 alloy. The loop density is about a factor of 3 less for the proton-irradiated case than for the neutron-irradiated case, which is expected since the proton irradiation temperature was optimized to track RIS (higher temperature) rather than the dislocation loop microstructure. That the loop sizes and densities are this close is somewhat remarkable considering that loop density is driven by in-cascade clustering, and cascades from proton irradiation are much smaller than those from neutron irradiation. However, the surviving fraction of interstitial loops is greater for proton irradiation, partially compensating the greater loop formation rate under neutron irradiation and resulting in loop densities that are within a factor of 3 [22].

Figure 11.20 shows the comparison of irradiation hardening between the two types of irradiation. The results are close, with proton irradiation resulting in slightly lower hardness. Figure 11.21 shows the IASCC susceptibility of CP 304 SS as measured by the %IG on the fracture surface following constant load testing (neutron-irradiated samples) and constant extension rate testing (proton-irradiated samples) in BWR normal water chemistry. Despite the significantly different testing mode, the results are in excellent agreement with that both proton and neutron irradiation result in the onset of IASCC at about 1 dpa (see Chap. 16).

In a study covering 11 solute addition alloys and 3 commercial alloys as part of the Cooperative IASCC Research (CIR) Program [23], the microstructure and properties of both proton and neutron irradiation were analyzed in which the latter was conducted in the BOR-60 reactor to doses between 4 and 47 dpa. Solute addition alloys consisted of controlled-purity heats of Fe–18Cr–12Ni to which single solute additions were made to test their effect on IASCC. Within this program, the grain boundary RIS of 6 solute addition alloys and 3 commercial alloys was measured following proton irradiation to 5.5 dpa (360 °C) or neutron

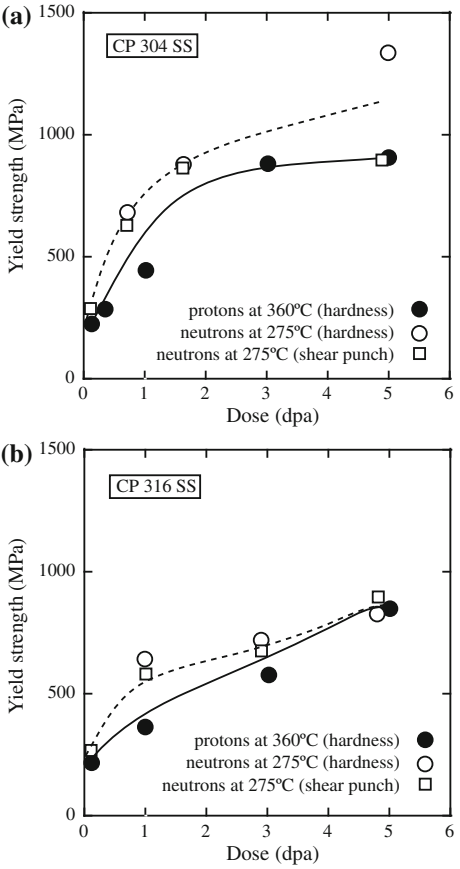

Fig. 11.20 Comparison of hardening in commercial purity (**a**) 304, and (**b**) 316 stainless steel irradiated with neutrons or protons to similar doses (after [21])

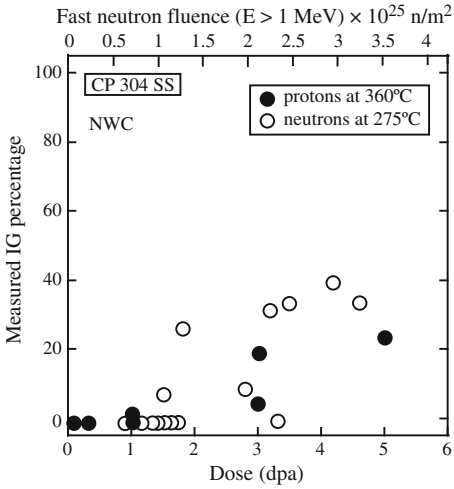

Fig. 11.21 Comparison of the extent of intergranular stress corrosion cracking in commercial purity 304 stainless steel following similar SCC tests of either neutron- or proton-irradiated samples from the same heat (after [21])

irradiation to between 5.4 and 11.8 dpa (320 °C). Figure 11.22 shows the agreement in grain boundary enrichment or depletion of Cr, Ni, Fe, Si, and Mo for these alloys. Proton and neutron irradiation under the selected conditions resulted in nearly identical elemental segregation behavior at grain boundaries [24]. The slightly higher temperature during proton irradiation was sufficient to increase diffusion kinetics and compensate for the increased damage rate.

The %IG cracking on the fracture surfaces was measured on both sample sets and results are shown in Fig. 11.23 as %IG relative to the reference Fe–18Cr–12Ni alloy without solute addition. As shown in the figure, the agreement is remarkable. Relative to the reference heat, the addition of either Ni, or Ni and Cr completely suppressed cracking in both neutron- and proton-irradiated samples. The addition of Mo produced no discernable effect on IG cracking in either of the irradiated samples. Finally, the addition of Si resulted in a substantial increase in %IG for both

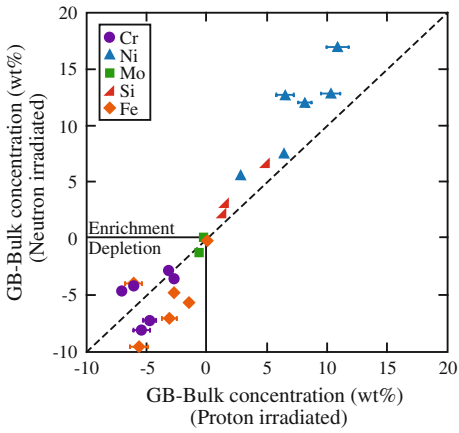

Fig. 11.22 Comparison of elemental enrichment and depletion from the bulk composition as a result of neutron and proton irradiation [24]

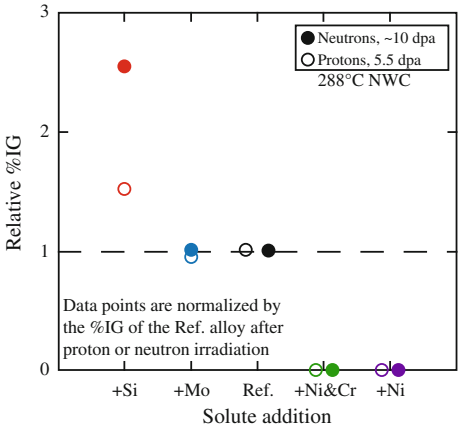

Fig. 11.23 Comparison of % IG after CERT testing of neutron- and proton-irradiated high-purity solute addition alloys tested in simulated BWR NWC [24]

irradiations. This agreement was perhaps the most notable of all of the existing data in that IASCC incorporates so many features in the irradiated microstructure. It also emphasized the importance of conducting experiments on the same heat of material to obtain a valid comparison by eliminating heat-to-heat variations.

Residual stresses are observed to relax under irradiation. Experiments were conducted on Inconel 718 following proton irradiation using 17 MeV protons at 300 °C [25] and on shot peened 304 followed by irradiation at 288 °C using 3.2 MeV protons to a dose of 2.0 dpa [26] and compared to respective results in reactor. In Inconel 718, the creep rate showed the expected linear dependence for applied shear stresses between 150 and 450 MPa. Stress relaxation amounted to about 30 % after a dose of 0.35 dpa, in good agreement with in-pile irradiation at 315 °C, Fig. 11.24(a) [27]. Results on 304 SS showed that the compressive stress

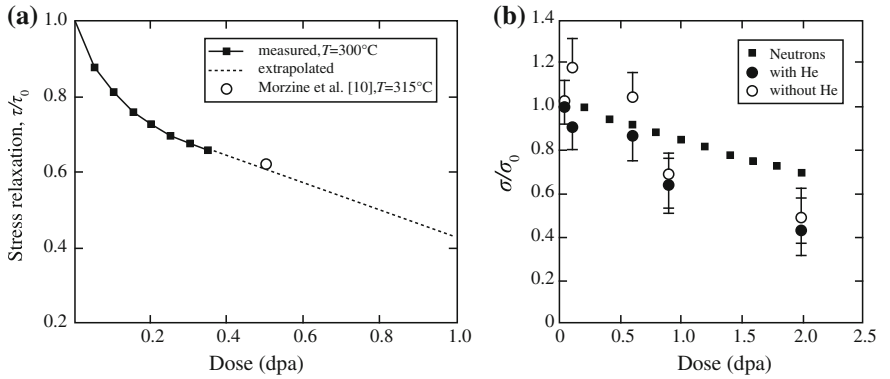

Fig. 11.24 Stress relaxation for (**a**) Inconel 718 after proton irradiation using 17 MeV protons at 300 °C [25] and compared with in-pile measurements at 315 °C [27], and (**b**) 304 SS irradiated with 3.2 MeV protons at 288 °C [26] and compared with neutron irradiation predictions [28]

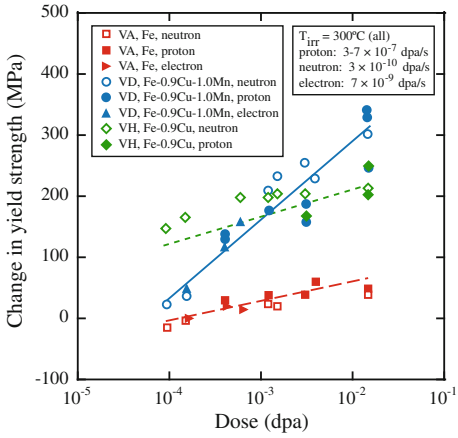

Fig. 11.25 Irradiation hardening in model reactor pressure vessel steels following neutron, proton, and electron irradiation at about 300 °C (after [29])

state was progressively relaxed throughout the dose range and that preinjection of helium did not significantly affect the relaxation, Fig. 11.24(b). A comparison of the results from proton irradiation and predictions based on neutron-induced relaxation of externally applied stresses [28] showed good agreement.

The next examples are from reactor pressure vessel steel, Zircaloy, and graphite. Figure 11.25 shows an experiment on model reactor pressure vessel alloys, in which the same heats were irradiated with neutrons, electrons, or protons at around 300 °C to doses spanning two orders of magnitude. The alloys include a high-purity Fe heat (VA) that hardens very little under irradiation, an Fe–0.9Cu (VH) heat that hardens rapidly initially, followed by a slower hardening rate above 0.1 mpda, and a Fe–0.9Ce–1.0Mn alloy (VD) in which the hardening rate is greatest over the dose range studied. Despite the very different compositions and hardening rates, the results of the three types of irradiation agree remarkably well.

Figure 11.26 shows hardening for Zircaloy-2 and Zircaloy-4 irradiated with either neutrons or protons. Although the irradiations were not conducted on the

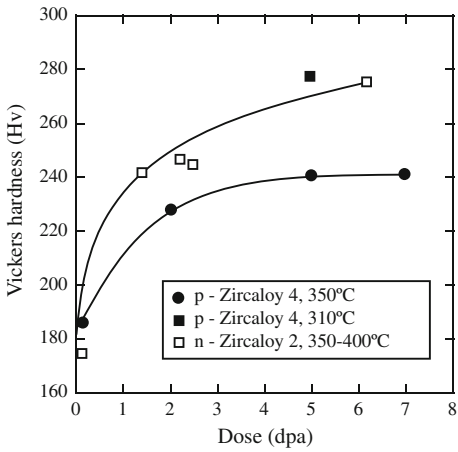

Fig. 11.26 Hardening of Zircaloy-4 irradiated with 3 MeV protons at 310 and 350 °C and comparison to neutron-irradiated Zircaloy-2 (after [30])

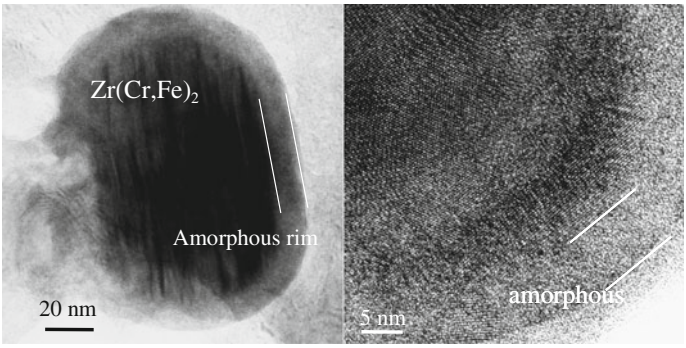

Fig. 11.27 Conventional (*left*) and high-resolution (*right*) image of a $Zr(Cr, Fe)_2$ precipitate after proton irradiation to 5 dpa at 310 °C, showing amorphization of the precipitate (after [30])

same heats of material, nor using similar irradiation parameters, there is good agreement in the magnitude and dose dependence of hardening. Figure 11.27 also shows proton-induced amorphization of a $Zr(Fe, Cr)_2$ precipitate after irradiation to 5 dpa at 310 °C, similar to that observed in reactor.

The corrosion kinetics of Zircaloy-4, both in-pile and out-of-pile, has been studied extensively to understand the role of irradiation on corrosion. Figure 11.28 shows oxide thickness data from the in situ irradiation–corrosion experiment [31] compared with in-pile data generated from MATPRO [32]. The unirradiated oxide growth rate of the reference sample (solid circles in red) was in good agreement with out-of-pile data. The proton irradiation data are also shown (solid squares in green) and the growth rate was about a factor of 10 higher than in the unirradiated case. Note that the growth rate was similar to that for in-pile behavior in the post-transition regime. In this regime, the oxide growth rate should be proportional to the dose rate. Therefore, equating the ratio of oxide growth rate to dose rate for

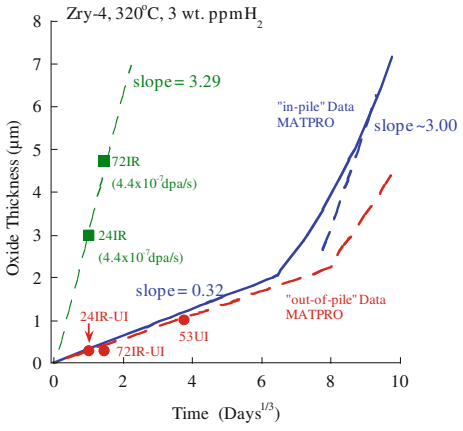

Fig. 11.28 Plot of oxide thickness as a function of corrosion time for in situ proton irradiation–corrosion data [31], and for in-pile and out-of-pile data [32]

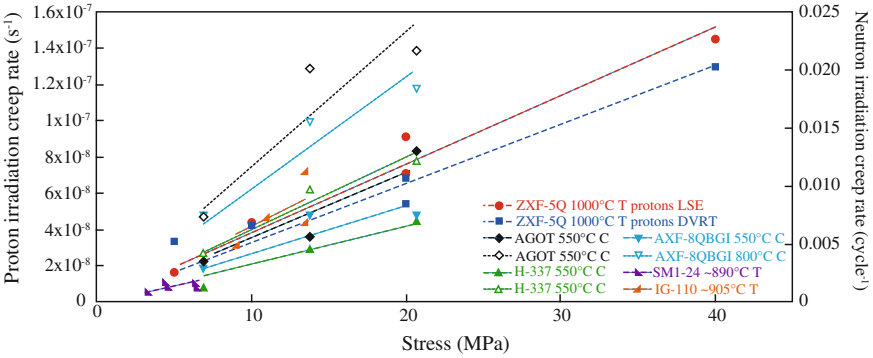

Fig. 11.29 Stress dependence of proton irradiation creep in ultra-fine grain graphite [33]

protons to that for neutrons yields a neutron damage rate of $\sim 4.4 \times 10^{-8}$ dpa/s, in good agreement with the range of values in the literature; $3.2–6.5 \times 10^{-8}$ dpa/s. This relationship suggested that oxidation under proton irradiation follows post-transition growth kinetics.

As discussed in Chap. 13, irradiation of samples under constant load can result in significant irradiation-induced creep. Proton irradiation creep experiments on ultra-fine grain graphite in the temperature range 900–1200 °C with stresses between 5 and 20 MPa and to a maximum dose of 1.0 dpa exhibited a linear dependence on the applied tensile stress, the dose rate and the temperature, and no dependence on the dose up to 1.0 dpa. Results were in excellent agreement with reactor creep experiments in the stress dependence of irradiation creep in graphite, Fig. 11.29. Both proton and neutron irradiation data show little dependence on temperature and dose rate, but the creep rates for proton irradiation were higher than those for reactor data by about an order of magnitude. Changes in the lattice parameters compared favorably with those after neutron irradiation at similar temperature and dose.

These examples represent a comprehensive collection of comparison data between proton and neutron irradiation and taken together, serve as a good example of the capability for charged particles to emulate the effect of neutron irradiation on the alloy microstructure. A more severe test of ion–neutron emulation is heavy ion irradiation at significantly higher dose rates as discussed next.

11.7 Emulation of Neutron Irradiation Damage with Self-Ion Irradiation

The challenge in using heavy- or self-ions to emulate neutron irradiation is greater than that for protons because of the issues listed in Sect. 11.4.2. However, the benefit is great since damage rates in the 10^{-4} to 10^{-2} dpa/s range can be achieved,

compressing the timescale to achieve several hundred dpa from decades (even in fast reactors) to hours. Very few experiments have been performed in which the microstructure or properties of heavy- or self-ion irradiations have been benchmarked against those from reactor irradiation. One such study [34] compared the full extent of the entire irradiated microstructure created in-reactor to that produced by self-ion irradiation designed to emulate that microstructure. Ferritic–martensitic alloy HT9 (Fe–12Cr–1Mo) heat 84425 was used in the hexagonal fuel bundle duct labeled ACO-3, in the Fast Flux Test Facility (FFTF). It was heat treated at 1065 °C/30 min/air cooled followed by 750 °C/60 min/air cooled. The fuel bundle was irradiated in several locations in FFTF over the time period 1985–1992 during which it accumulated a total damage of about 155 dpa at an average temperature of 443 °C [35]. Pieces from an archival section of this same duct were irradiated in a 1.7 MV tandem accelerator with self-ions (Fe^{++}) at 5 MeV at a temperature of 460 °C and to a dose of 188 dpa determined using SRIM [36] in the Kinchin-Pease mode [37]. At this energy, Fe^{++} ions come to rest at a depth of approximately 1.6 μm below the surface. The ion irradiation temperature represents a 17 °C increment above the neutron irradiation temperature, as predicted by invariance theory [38]. To emulate transmutation in reactor, helium was implanted prior to ion irradiation to a concentration of 1 appm over a depth range of 300–1000 nm by varying the implantation energy over five different values. This amount of He was set below that generated in reactor to compensate for the initially high He/dpa ratio in the ion irradiation experiment.

Figure 11.30(a–d) shows the pairs of images of each microstructure feature (dislocation loops, precipitates, and voids) characterized in both ion- and reactor-irradiated samples of HT9 heat 84425. Qualitatively, the microstructures

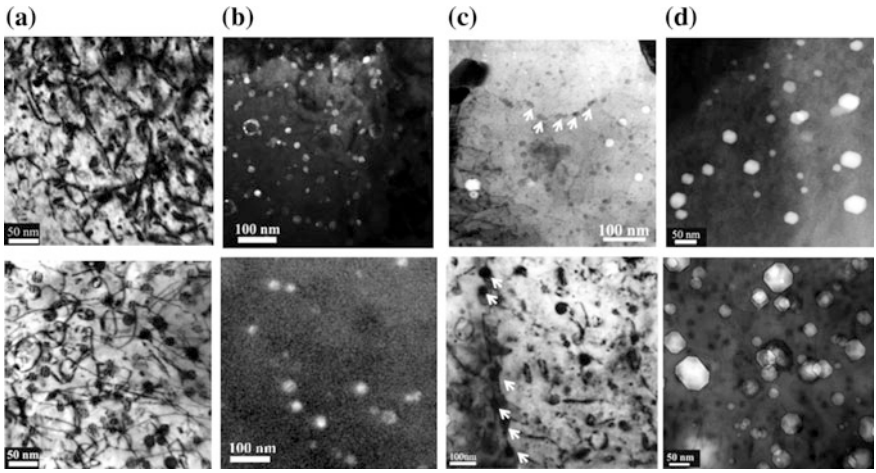

Fig. 11.30 Comparison of irradiation microstructure in HT9 following Fe^{++} irradiation (460 °C:188 dpa with 1 appm helium, *top images*) and following reactor irradiation in FFTF (443 °C:155 dpa, *bottom images*): (**a**) bright field TEM images of line dislocations and loops, (**b**) dark field TEM images of G-phase precipitates in the matrix, (**c**) bright field images of G-phase precipitates along grain boundaries, and (**d**) voids (after [34])

showed all the same radiation-produced features. In both cases, the dislocation microstructure consists of dislocation line segments ($a\langle 100\rangle$ and $(a/2)\langle 111\rangle$) and loops, predominantly $a\langle 100\rangle$ type, of similar diameter ($\sim$20 nm) and number density ($5–9 \times 10^{20}$ m^{-3}) (Fig. 11.30(a)). Radiation-induced precipitates were primarily the G-phase as shown in the dark field TEM image (Fig. 11.30(b)) and a Cr-rich phase (not shown). The composition of the G-phase was confirmed by APT to be close to $Mn_6Ni_{16}Si_7$. G-phase precipitates also appeared along grain boundaries in both cases, as shown in the TEM bright field images in Fig. 11.30(c). The Cr-rich phases under reactor irradiation contained only Cr, and those irradiated with Fe^{++} consisted of Cr with a few percent carbon. Void formation was very heterogeneous in both reactor and Fe^{++}-irradiated samples, with large variations between grains and laths. However, the size and the number density were similar (Fig. 11.30(d)).

A quantitative comparison of defect size and number density as a ratio of ion irradiation to reactor irradiation is shown in Fig. 11.31. The void swelling was nearly identical between the two irradiations, and the size and the density of precipitates and loops following ion irradiation were within a factor of two of those for reactor irradiation. Results indicated that as predicted by invariance theory, the reactor-irradiated microstructure can be emulated by ion irradiation with only a modest temperature increment (17 °C). The damage increment (33 dpa) over the reactor irradiation was also small. These results indicate that an Fe^{++} irradiation at 460 °C with preinjection of 1 appm He emulates the irradiated microstructure, both qualitatively and quantitatively (within a factor of two), created by fast reactor irradiation at an average temperature of 443 °C and to a similar damage level.

A set of experiments similar to that for F-M steel was conducted on solution annealed 304L SS from a core shroud, and cold worked 316 SS from a baffle bolt [39]. Both steels were irradiated in the BOR-60 reactor to doses of 5.4, 10.3, and 46 dpa. Archive material from both heats was irradiated with 5 MeV Ni^{++} ions at temperatures and doses of 380 °C:46 and 260 dpa, 500 °C:46 dpa, and 600 °C:46 dpa. Ni^{++} ion irradiation at 380 °C produced a dislocation loop microstructure close to that by neutron irradiation at 320 °C in terms of loop size

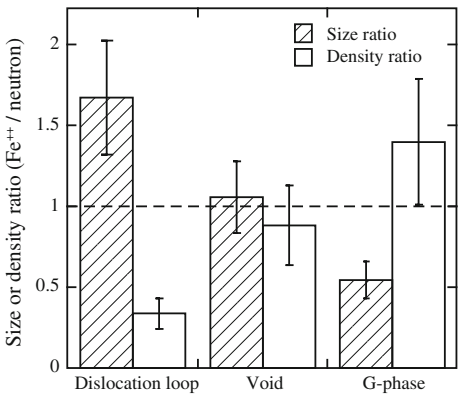

Fig. 11.31 Comparison of size and number density ratios of defect clusters for ion and neutron irradiation under similar conditions (after [34])

and density for the 304L SS. For the 316L SS, the dislocation loop density was a factor of 4 lower that that in reactor and no SFTs were observed.

Ni/Si-rich clusters were observed in self-ion-irradiated 304L SS (5 MeV Fe^{++}) at 380 °C:46 dpa and they were likely precursors of G-phase. Some of the Ni/Si-rich clusters reached the composition of G-phase at 260 dpa [40]. However, the precipitate size was smaller and the density was lower compared to neutron irradiations at 320 °C to 46 dpa, indicating that a temperature shift larger than 60 °C may be needed for SA 304L SS to exhibit a comparable G-phase morphology. G-phase precipitates were observed in cold worked 316 SS following self-ion irradiation to 46 dpa at 380 °C, although most of the Ni/Si-rich clusters were still in the precursor stage. Considering only the G-phase particles, the average size was ~4 nm and the number density is estimated to be 0.1×10^{23} m^{-3}. The average size of precipitates by self-ion irradiations at 380 °C:46 dpa was slightly smaller than those found in neutron irradiated same heat of samples at 320 °C:46 dpa (~5 nm) but at higher density (number density in neutron-irradiated samples was reported to be $<0.1 \times 10^{23}$ m^{-3}). The temperature shift for cold worked 316 SS appeared to be smaller than that of solution annealed 304L SS probably due to the high density of dislocations, which served as defect sinks and mitigated the effect of high dose rate.

Radiation-induced segregation in cold worked 316 SS by heavy ion irradiation at 380 °C was comparable to that by neutrons at 320 °C. The modest temperature shift for RIS in this alloy may be due to the highly deformed microstructures, which consist of high density of defect sinks. There was substantial difference in the magnitude of segregation between ion and neutron irradiation to similar doses in the SA 304L SS alloy with less segregation in ion irradiation than in neutron irradiation. Increasing the temperature to 500 °C increased the magnitude of segregation but the widths of the enriched or depleted zones were much larger at the higher temperature. Results appear to follow the invariance relations, which predict that larger temperature shifts are required to match RIS than the loop or void microstructure.

Nomenclature

C_i	Concentration of atom of type i
E_d	Displacement energy
k_S^2	Sink strength
$l(t)$	Half width of the chromium-depleted zone
M	Amount of grain boundary chromium depletion defined by Eq. (11.5)
N_S	Number of defects per unit volume lost to sinks
N_R	Number of defects per unit volume lost to recombination
R_S	Ratio of vacancy loss to interstitial loss
T	Energy transferred
$P(T)$	Fraction of recoils between E_d and T
$W(E_i, T)$	Weighted average recoil spectrum
$\sigma(E_i, T)$	Scattering cross section for the transfer of energy in $T + dT$
$\sigma_D(E_i)$	Displacement cross section

Acronyms

AES	Auger electron spectroscopy
APT	Atom probe tomography
CP	Commercial purity
IASCC	Irradiation-assisted stress corrosion cracking
IGSCC	Intergranular stress corrosion cracking
K–P	Kinchen–Pease
NRT	Norgett, Robinson, Torrens
SCC	Stress corrosion cracking
SRIM	Stopping power and ranges of ions in matter
STEM-EDS	Scanning transmission electron microscopy-energy dispersive spectroscopy

Problems

11.1 Radiation effects experiments can be conducted with a variety of energetic particles. However, the result is sometimes dependent on the nature of the irradiating particle and the conditions under which the irradiation occurs.

(a) Explain (as quantitatively as possible) the differences in the effects of irradiation for a 1 MeV particle of the following types: electron, proton, neutron, and Ni ion. In your answer, make sure you address the following:

(i) The recoil spectrum
(ii) The damage function
(iii) The spatial distribution of defects and the form of the defects
(iv) The subsequent behavior of freely migrating defects and defect clusters.

(b) Unfortunately, irradiations with the various types of particles do not occur under identical conditions. The following are typical temperatures and dose rates for irradiation with each particle type, as dictated by the facility needed to produce such particles:

Electrons: 500 °C, 10^{-3} dpa/s
Protons: 400 °C, 10^{-5} dpa/s
Ni ions: 500 °C, 10^{-3} dpa/s
Neutrons: 300 °C, 10^{-8} dpa/s
Answer part (a) again given these irradiation conditions.

11.2 Three separate particles travel through a pure iron slab, specifically 1 MeV neutrons, 1 MeV gammas, and 1 MeV electrons. For each:

(a) Calculate the maximum possible energy transfer to an Fe atom from each particle.
(b) State any assumptions you made in part (a).
(c) Explain the relative damage consequences for each particle.
(d) To minimize damage to the iron, would it be a good idea to place shielding between the radiation source and the iron slab?

11.3 Calculate and graph the weighted recoil spectra for 1 MeV protons and 1 MeV neutrons incident on copper.

11.4 Using the invariance requirements, determine the temperature at which proton irradiations should be conducted in order to produce:

(a) The same amount of RIS
(b) The same dislocation microstructure as irradiation in a fast reactor at a temperature of 500 °C, given that the proton damage rate is 10^{-5} dpa/s and the damage rate in a fast reactor is 8×10^{-8} dpa/s. Use $E_m^v = 1.3$eV; $E_f^m = 1.9$eV.

11.5 Determine the optimum ion irradiation technique for the following objectives:

(a) High-dose (100 dpa) microstructure investigation of stainless steel at high (500 °C) temperature
(b) Investigation of the effect of irradiation on SCC of a zirconium alloy in water
(c) Tracking the evolution of amorphization with dose.

References

1. Abromeit C (1994) J Nucl Mater 216:78–96
2. Mazey DJ (1990) J Nucl Mater 174:196
3. Active Standard (1989) Standard practice for neutron irradiation damage simulation by charged particle irradiation, designation E521-89. American Standards for Testing and Materials, Philadelphia, p D-9
4. Was GS, Andresen PL (1992) JOM 44(4):8
5. Andresen PL, Ford FP, Murphy SM, Perks JM (1990) In: Proceedings of the 4th international symposium on environmental degradation of materials in nuclear power systems: water reactors. National Association of Corrosion Engineers, Houston, pp 1–83
6. Andresen PL (1992) In: Jones RH (ed) Stress corrosion cracking, materials performance and evaluation. ASM International, Metals Park, p 181
7. Sterbentz JW (2004) Neutronic evaluation of a 21 × 21 supercritical water reactor fuel assembly design with water rods and SiC clad/duct materials, INEEL/EXT-04-02096, Idaho National Engineering and Environmental Laboratory. Bechtel BWXT Idaho, LLC, Idaho Fall, ID

8. Kinchin GH, Pease RS (1955) Prog Phys 18:1
9. Norgett MJ, Robinson MT, Torrens IM (1974) Nucl Eng Des 33:50
10. Was GS, Allen T (1993) J Nucl Mater 205:332–338
11. Perks JM, Marwick AD, English CA (1986) AERE R 12121 June
12. Was GS, Allen TR (2007): In: Sickefus KE, Kotomin EA, Obervaga BP (eds) Radiation effects in solids, NATO science series II: mathematics, physics and chemistry, vol 235. Springer, Berlin, pp 65–98
13. Ezawa T, Wakai E (1991) Ultramicroscopy 39:187
14. Ashworth JA, Norris DIR, Jones IP (1992) JNM 189:289
15. Wakai E (1992) Trans JIM 33(10):884
16. Whitley JB (1978) Dissertation. Nuclear engineering, University of Wisconsin-Madison
17. Garner FA (1983) J Nucl Mater 117:177–197
18. Lee EH, Mansur LK, Yoo MH (1979) J Nucl Mater 85(86):577–581
19. Brailsford AD, Mansur LK (1977) J Nucl Mater 71:110–116
20. Ziegler JF, Biersack JP, Littmark U (1996) The stopping and range of ions in matter. Pergamon, New York
21. Was GS, Busby JT, Allen T, Kenik EA, Jenssen A, Bruemmer SM, Gan J, Edwards AD, Scott P, Andresen PL (2002) J Nucl Mater 300:198–216
22. Gan J, Was GS, Stoller R (2001) J Nucl Mater 299:53–67
23. Scott P (2003) Materials reliability program: a review of the cooperative irradiation assisted stress corrosion cracking research program (MRP-98), 1002807, Palo Alto, CA
24. Stephenson KJ, Was GS (2015) J Nucl Mater. 456:85–98
25. Scholz R, Matera R (2000) J Nucl Mater 414:283–287
26. Sencer BH, Was GS, Yuya H, Isobe Y, Sagasaka M, Garner FA (2005) J Nucl Mater 336:314–322
27. Baicry J, Mardon JP, Morize P (1987) In: Adamson RB, van Swam LFP (eds) Proceedings on seventh international symposium on Zirconium in the nuclear industry, STM STP 939, American Society for Testing and Materials, West Conshohocken, PA, p. 101
28. Garner FA (1994) Irradiation performance of cladding and structural steels in liquid metal reactors. In: Frost BRT (ed) Materials science and technology: a comprehensive treatment (Chapter 6), vol 10A. VCH, New York, p 419
29. Was GS, Hash M, Odette GR (2005) Phil Mag 85(4–7):703–722
30. Zu XT, Sun K, Atzmon M, Wang LM, You LP, Wan FR, Busby JT, Was GS, Adamson RB (2005) Phil Mag 85(4–7):649–659
31. Wang P, Was GS (2015) J Mater Res 30(9):1335–1348
32. Allison CM et al, MATPRO-A library of materials properties for light-water-reactor accident analysis, NUREG/CR-6150, EGG-2720, vol 4, pp 4–234
33. Campbell A, Campbell KB, Was GS (2013) Carbon 60:410
34. Was GS, Jiao Z, Getto E, Sun K, Monterrosa AM, Maloy SA, Anderoglu O, Sencer BH, Hackett M (2014) Scr Mater 88:33
35. Sencer BH, Kennedy JR, Cole JI, Maloy SA, Garner FA (2009) J Nucl Mater 393:235
36. Ziegler JF, Ziegler MD, Biersak JP (2010) Nucl Instr Meth Phys Res B 268:1818
37. Stoller RE, Toloczko MB, Was GS, Certain AG, Dwaraknath S, Garner FA (2013) Nucl Instr Meth Phys Res B 310:75
38. Mansur LK (1978) Nucl Technol 40:5
39. Was GS, Jiao Z, Van der ven A, Buremmer S, Edwards D (2012) Aging and embrittlement of high fluence stainless steels, final report, NEUP project CFP-09-767, December 2012
40. Jiao Z, Was GS (2014) J Nucl Mater 449:200